ACS APPLIED ELECTRONIC MATERIALS

pubs.acs.org/acsaelm Article

# Multiferroic Self-Assembled $BaTiO_3$−Fe Vertically Aligned Nanocomposites on Mica Substrates toward Flexible Electronics

Juncheng Liu, Xuejing Wang, Han Wang, Zhimin Qi, James P. Barnard, Bruce Zhang, and Haiyan Wang*

Cite This: *ACS Appl. Electron. Mater.* 2022, 4, 4077−4084 Read Online

ACCESS | Metrics & More | Article Recommendations | Supporting Information

Downloaded via PURDUE UNIV on March 29, 2023 at 03:06:41 (UTC).
See https://pubs.acs.org/sharingguidelines for options on how to legitimately share published articles.

**ABSTRACT:** Integration of functional thin films with a multiferroic property on flexible substrates has piqued tremendous research interest and device potential for flexible electronics. In this work, self-assembled $BaTiO_3$−Fe vertically aligned nanocomposite (VAN) thin films have been integrated on mica substrates using pulsed laser deposition. Different buffer layers have been explored to facilitate VAN growth. The anisotropic ferromagnetic property and room temperature ferroelectric property have been achieved in the films. The bending test up to 1000 cycles signifies the mechanical stability of the physical properties. This work paves an avenue to integrate multiferroic oxide−metal nanocomposites for future flexible device integration.

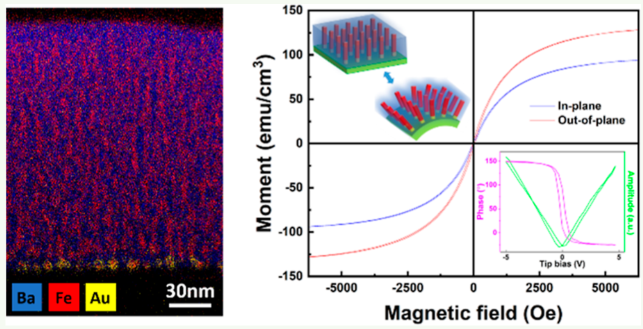


**KEYWORDS:** *multiferroic, flexible electronics, oxide−metal vertically aligned nanocomposite, pulsed laser deposition, mica*

## ■ INTRODUCTION

Multiferroic thin films have attracted great interests owing to the potential for applications in low-power logic-memory devices, radio- and high-frequency devices, high-sensitivity magnetic field sensors, and photocatalysis.[1−7] Several multiferroic single-phase oxides have been well explored, including $BiFeO_3$, $YMnO_3$, and $Fe_3O_4$.[8−12] Driven by the need to improve the magnetoelectric coupling behavior, artificial composite multiferroic systems with different microstructures have been studied, including particulate composites, laminated multilayer thin films, and vertically aligned nanocomposites (VANs).[13−19] A VAN is a composite containing two or more phases, where one phase grows as nanopillars within the other phase, which grows as the matrix. Such a structure presents the advantages of achieving out-of-plane anisotropy in the magnetic property, easy tuning multiferroic, and other properties by structural and strain tuning, as well as the potential toward integrating other functionalities such as optical and plasmonic properties.[20−29] Most of the multiferroic nanocomposites have been integrated on single-crystalline oxide substrates with limited success on other substrates such as Si(001).[30−33]

Inspired by the needs of wearable flexible electronic devices and the enormous functionality potential of oxides, the integration of functional oxide thin films on flexible substrates has been attractive.[34−39] To achieve such integration, one way is via wafer transfer, i.e., the film was first deposited on a rigid substrate, followed by transferring the film to other flexible substrates, such as polymers.[40,41] However, this method is complicated, which requires multiple steps. An alternative is directly integrating the functional thin film on a flexible substrate. Among all the flexible substrates, mica has been proven to be an outstanding candidate. It is easy to be peeled off and possesses multiple advantages such as low cost, light weight, and excellent thermal stability and mechanical property. Several functional oxide thin films have been reported to grow on mica for future device applications.[42−44] Recently, several oxide−oxide VAN systems have been demonstrated for mica integration toward flexible electronics.[45,46] The reports on the integration of oxide−metal VAN systems on mica are very limited,[47,48] as shown in Table 1 for the list of recently reported VAN systems on mica. This is largely due to the growth incompatibility and limited buffer layer selections. Up to date, there is no prior report on the integration of ferromagnetic and ferroelectric properties in oxide−metal VAN systems integrated on mica.

In this work, we demonstrate self-assembled $BaTiO_3$ (BTO)−Fe VAN thin films grown on muscovite mica substrates with the goal to achieve a multiferroic nanocomposite for flexible multifunctional devices. BTO is selected considering its ferroelectric nature, while Fe is a well-known ferromagnetic material.[49] Such BTO−Fe VAN system has been previously deposited on $SrTiO_3$ substrates and single-

**Received:** May 31, 2022
**Accepted:** July 18, 2022
**Published:** August 11, 2022

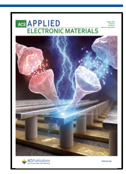

ACS Publications © 2022 American Chemical Society

**Table 1. List of Reported VAN Systems Integrated on Mica and Their Properties**

| VAN system | Type of VAN | Functionalities | Refs |
|---|---|---|---|
| $BiFeO_3$−$CoFe_2O_4$ on mica | oxide−oxide | ferrimagnetic, ferroelectric, multiferroic | 45 |
| $La_{0.67}Sr_{0.33}MnO_3$−NiO on mica | oxide−oxide | exchange bias | 46 |
| $BaTiO_3$−Au on mica | oxide−metal | plasmonic, hyperbolic | 47 |
| $BaZrO_3$−Co on mica | oxide−metal | ferromagnetic | 48 |
| $BaTiO_3$−Fe on mica | oxide−metal | ferromagnetic, ferroelectric, multiferroic | this work |

crystalline Si.[30,33] To enable its epitaxial growth and enhance the pillar alignment in oxide−metal VAN, different buffer layers have been explored to compare the epitaxial growth quality on mica. Magnetic and ferroelectric property measurements have been performed to characterize the multiferroic nature of the films. Considering its anisotropic microstructure of VAN nanocomposites, optical properties, including transmittance and ellipsometry measurements, have been carried out for multifunctionality demonstration. The cyclic bending test has also been conducted to examine the mechanical stability of the nanostructures and their physical properties.

## RESULTS AND DISCUSSION

To facilitate the growth of BTO−Fe VAN on mica substrates, different buffer layers have been explored since no obvious VAN structure could be obtained for the direct growth of BTO−Fe on mica, as shown in Figure S1. The BTO−Fe film was first deposited on mica with a BTO buffer layer since BTO has been demonstrated with successful growth on mica.[50] The microstructure of the films was characterized by STEM and EDS, as summarized in Figure 1. The vertical growth of segmented Fe nanopillars within the BTO matrix is confirmed, with some of the Fe nanostructures grown as nanoparticles. In order to further improve the Fe nanopillar growth quality, a BTO−Au nanocomposite interlayer was introduced between the film and the substrate, since such a BTO-Au VAN system has been demonstrated successfully on mica.[47] As shown in Figure 2, the Fe nanopillar growth quality has been obviously improved compared to the one with BTO buffer (Figure 1). Here, the BTO−Au layer (around 5 nm thick) was first deposited on a mica substrate, where Au grew as islands within the BTO matrix. The Au islands could then serve as nucleation sites to facilitate the Fe nucleation, which results in better alignment of Fe nanopillars. The estimated diameter of thin Fe nanopillars for the two films is around 2 nm. The ratio between BTO and Fe is close to 1:1, as suggested by the EDS mapping shown in Figure S2. X-ray diffraction was conducted to investigate the crystallinity of the BTO−Fe thin films, as summarized in Figure S3. BTO shows (110) dominant growth with a small portion of (111) oriented growth. The $2\theta$ value of BTO (110) is 30.96° for the BTO−Fe/BTO/mica and 30.89° for BTO−Fe/BTO−Au/mica film, with a tensile strain calculated to be 1.3% and 1.5% for BTO in the two films. It is noted that the Fe peaks could be potentially overlapped with mica (00*l*) peaks for both films. Au grows mostly in the (111) orientation for the BTO−Fe/BTO−Au/mica film, which is consistent with previous reports of the BTO−Au film grown on mica. The mechanism of formation of the BTO−Fe VAN structure could be explained as follow: Fe adatoms nucleate and diffuse into islands following the Volmer−Weber mode due to their higher surface energy (~2.40 J/$cm^2$), while BTO adatoms prefer the Frank−van der Merve mode for a layer-by-layer growth owing to their lower surface energy (~1.24 J/$cm^2$). After nucleation, BTO and Fe adatoms further diffuse and nucleate to form an overall VAN structure with an Fe pillar embedded in the BTO matrix. A photo of the BTO−Fe/BTO/mica sample when bent convexly is shown in Figure 1j, indicating the flexibility of the samples.

To investigate the magnetic properties of the BTO−Fe films, in-plane and out-of-plane magnetic properties at room temperature have been measured, as the $M$−$H$ curves plotted in Figure 3a,b. Both the BTO−Fe/BTO/mica and BTO−Fe/

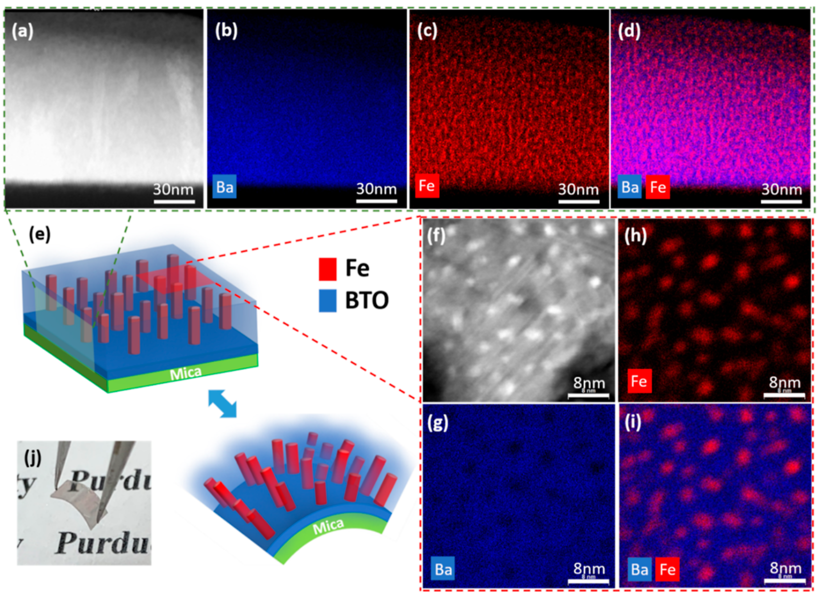


**Figure 1.** Cross-sectional (a) HAADF STEM image and EDS mapping of BTO−Fe/BTO/mica film for (b) Ba, (c) Fe, and (d) Ba/Fe. (e) Schematic drawing of the BTO−Fe/BTO/mica film when flat and bent convexly. Plan-view (f) HAADF STEM image and EDS mapping of the BTO−Fe/BTO/mica film for (g) Ba, (h) Fe, and (i) Ba/Fe. (j) Photo of the BTO−Fe/BTO/mica sample when bent convexly.


https://doi.org/10.1021/acsaelm.2c00712
ACS Appl. Electron. Mater. 2022, 4, 4077−4084

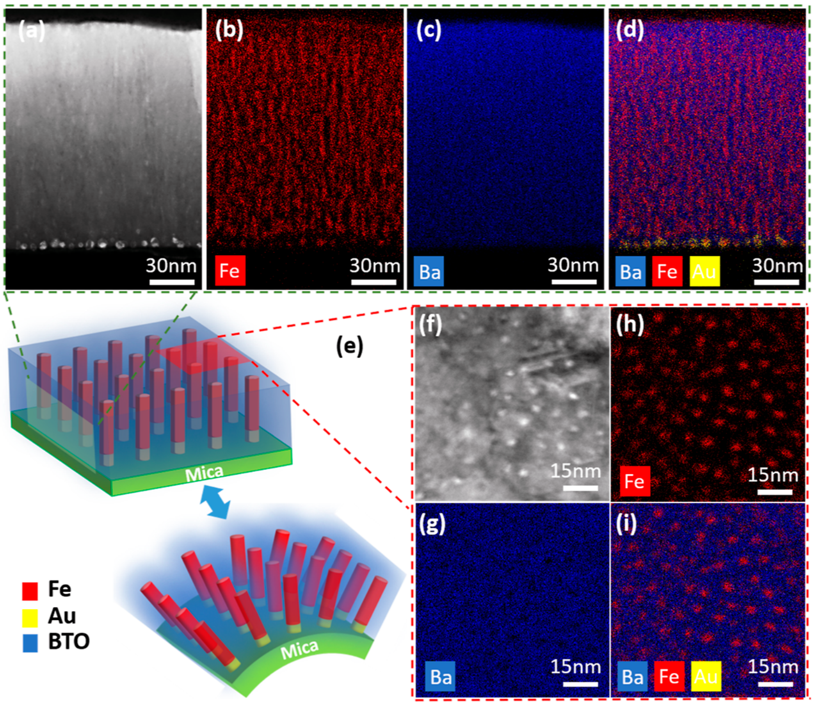


Figure 2. Cross-sectional (a) HAADF STEM image and EDS mapping of the BTO−Fe/BTO−Au/mica film for (b) Ba, (c) Fe, and (d) Ba/Fe. (e) Schematic drawing of the BTO−Fe/BTO/mica film when flat and bent convexly. Plan-view (f) HAADF STEM image and EDS mapping of the BTO−Fe/BTO−Au/mica film for (g) Ba, (h) Fe, and (i) Ba/Fe.

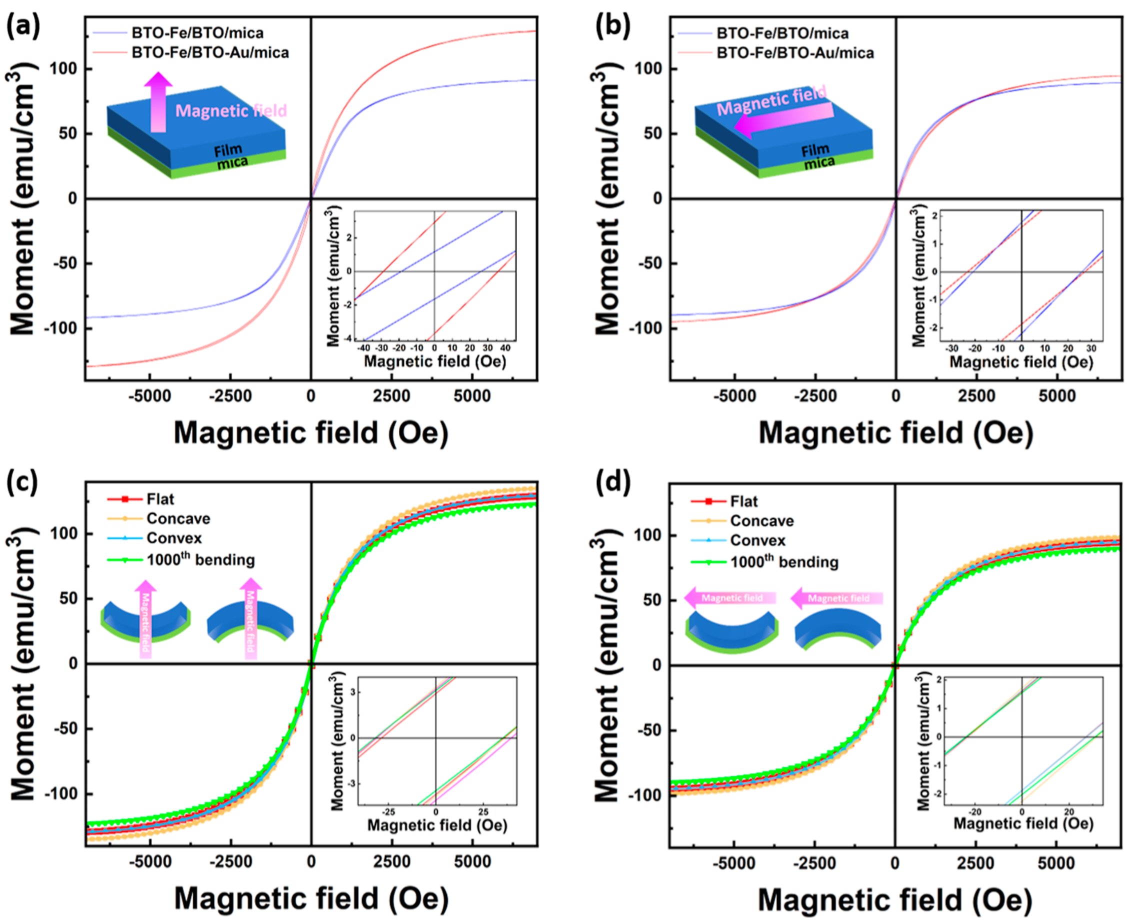


Figure 3. (a) Out-of-plane and (b) in-plane $M-H$ curves for the BTO−Fe/BTO/mica and BTO−Fe/BTO−Au/mica films. (c) Out-of-plane and (d) in-plane $M-H$ curves for the BTO−Fe/BTO−Au/mica film under different bending conditions.


https://doi.org/10.1021/acsaelm.2c00712
ACS Appl. Electron. Mater. 2022, 4, 4077−4084

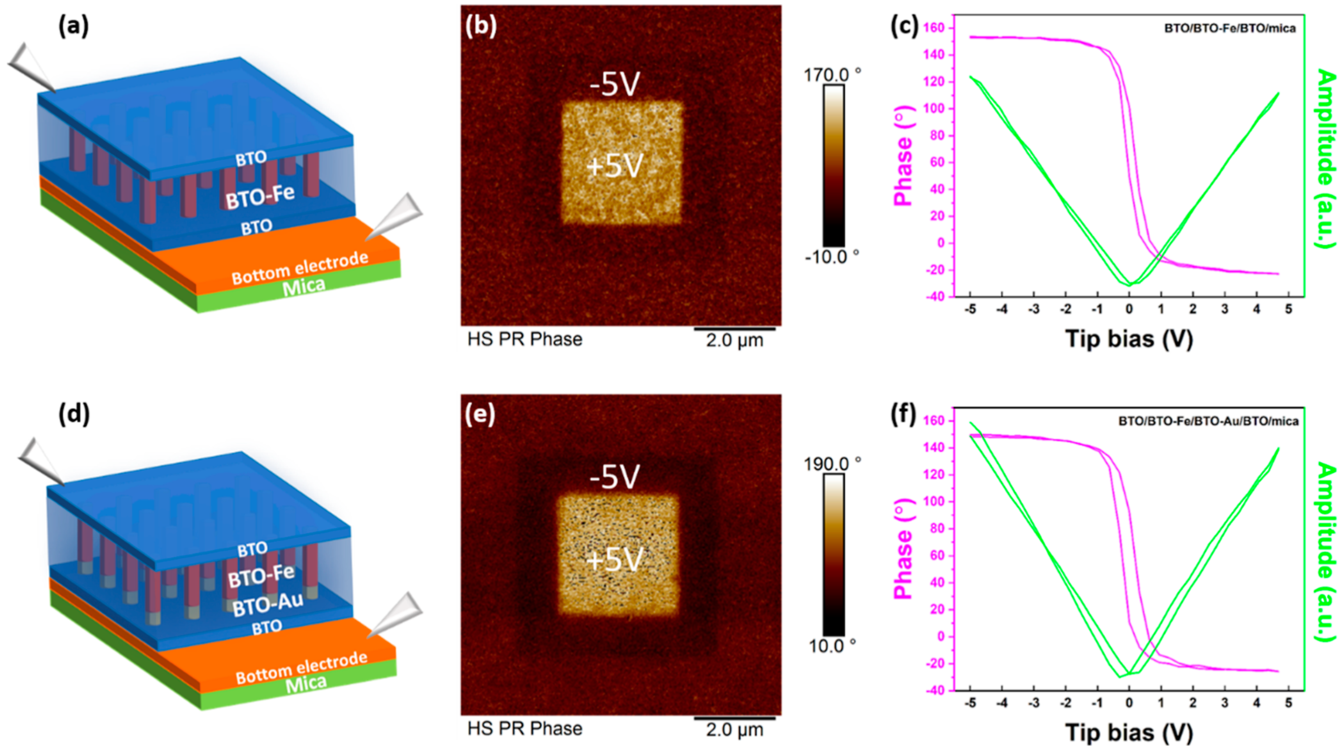


**Figure 4.** Schematic drawing of the (a) BTO/BTO−Fe/BTO and (d) BTO/BTO−Fe/BTO−Au/BTO multilayer design. (b), (e) PFM phase mapping for the two films. (c,f) Phase and amplitude hysteresis loops of PFM measurements for the two films.

BTO−Au/mica films show soft ferromagnetic behavior. More specifically, the saturation moments are 93 and 129 emu/cm$^3$, while the coercive fields are 23 and 32 Oe for the BTO−Fe/BTO/mica and BTO−Fe/BTO−Au/mica film out-of-plane. For the in-plane measurement, the saturation moments are 90 and 95 emu/cm$^3$, and the coercive fields are 24 and 25 Oe for the two films. A stronger ferromagnetic response and a more obvious magnetic anisotropy could be observed for the BTO−Fe/BTO−Au/mica film compared to the BTO-buffered one, which could be attributed to the better crystallinity quality of Fe pillars and improved vertical alignment within the film than that of the BTO-buffered film. The magnetic anisotropy of the film is primarily from the shape anisotropy of Fe pillars considering the high aspect ratio of the nanopillars (length/diameter ∼ 60). It is noted that both films show a low coercivity, probably due to the very thin (around 2 nm in diameter) Fe nanopillars within the film.

Since the films are integrated on flexible mica substrates, it is important to test the stability of the physical properties under different bending conditions. The magnetic property measurement was performed when bent concavely, convexly, and after 1000th bending for the BTO−Fe/BTO−Au/mica film, and in-plane and out-of-plane direction were both also tested, as summarized in Figure 3c,d. Local regimes of the plots are shown in Figure S4. The bending radius during the bending test was around 15 mm. It is interesting that no obvious difference was observed for the results measured at different bending conditions for both in-plane and out-of-plane directions, indicating a stable ferromagnetic property of the film against the bending test. The saturation moment and coercive field stay around 129 emu/cm$^3$ and 32 Oe for the out-of-plane measurement and 95 emu/cm$^3$ and 25 Oe for in-plane measurement, respectively. The results indicate the reliability and robustness of the nanocomposite thin films. The minor difference in the measured magnetic moments under different bending conditions could be owing to the minor sample geometry changes and measurement limitations. It is noted that the volume used to calculate the magnetic moment of the film was the entire film volume rather than Fe pillars. The actual magnetization of Fe region should be even stronger.

Considering their potential ferroelectric property, piezoelectric force microscopy (PFM) analysis was carried out for both systems at room temperature. Films were sandwiched by two BTO layers to form BTO/BTO−Fe/BTO−Au/BTO/mica and BTO/BTO−Fe/BTO/mica multilayers, as shown in the schematic drawings in Figure 4a,d. The thickness of the BTO layers is around 5 nm. The films were first written by −5 V on an area of 5 × 5 $\mu$m, followed by a rewriting process by +5 V on the center 3 × 3 $\mu$m area. Both films show obvious dark and bright contrast, as displayed in Figure 4b,e as the piezo-response phase mappings, which indicate the upward and downward polarizations. The phase hysteresis loops in Figure 4c,f suggest that both films present a 180° phase change by switching the tip bias direction, while the amplitude hysteresis loops show a well-defined butterfly shape, which signifies strong ferroelectric response for both films. The polarization−voltage measurement was performed for the BTO/BTO−Fe/BTO−Au/BTO/mica film. As plotted in Figure S5, the result shows a well-defined polarization−voltage hysteresis loop, suggesting a room-temperature ferroelectric property of the film. The cyclic bending tests and PFM measurements were conducted on samples, as shown in Figure S6. Both films show stable ferroelectric properties after 1000th bending. The results demonstrate that both BTO−Fe/BTO−Au/mica and BTO−Fe/BTO/mica film present a stable, room temperature ferroelectric property. A leakage current measurement was performed on the BTO/BTO−Fe/BTO−Au/BTO/mica film, as shown in Figure S7. The leakage current of the



https://doi.org/10.1021/acsaelm.2c00712
ACS Appl. Electron. Mater. 2022, 4, 4077−4084

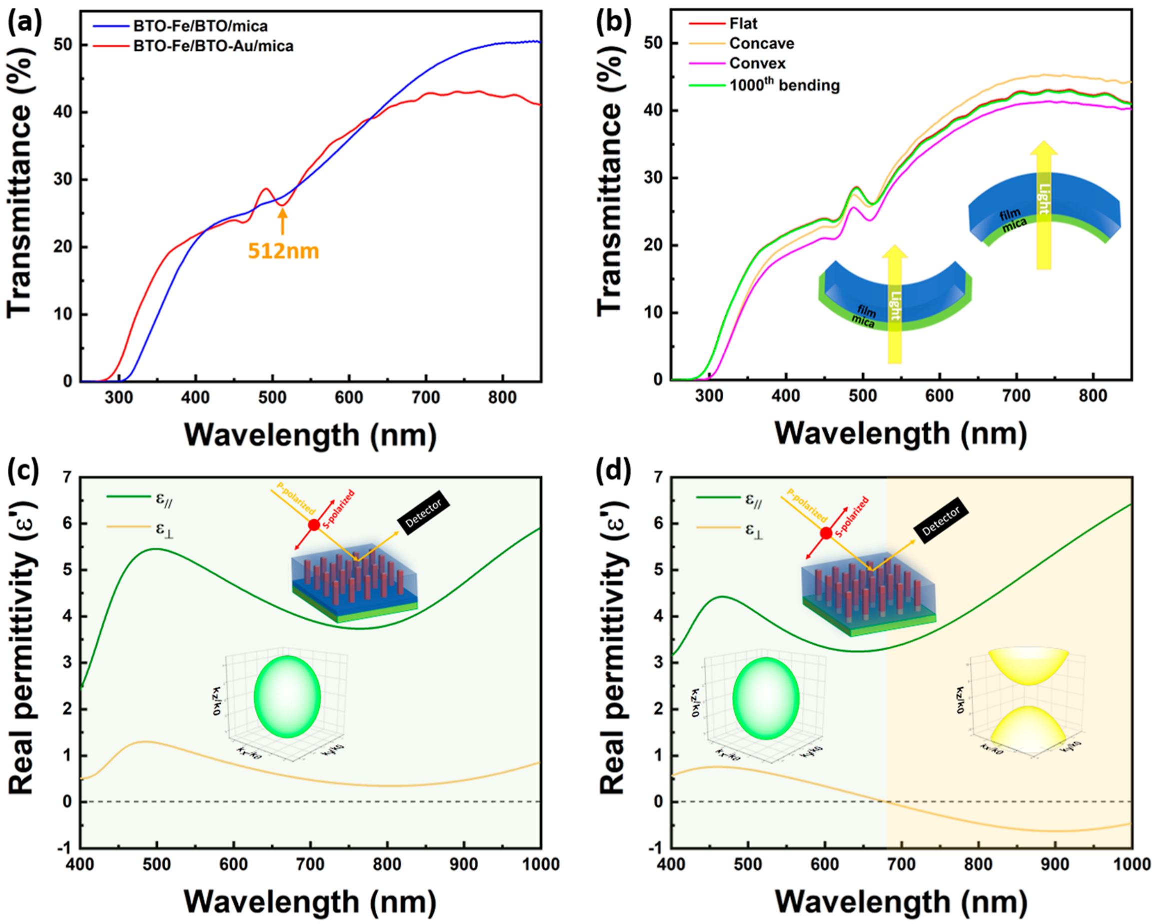


**Figure 5.** (a) Transmittance plots for the BTO−Fe/BTO/mica and BTO−Fe/BTO−Au/mica films. (b) Transmittance plots for the BTO−Fe/BTO−Au/mica film measured when flat, bent concavely and convexly, as well as after 1000th bending cycles. (c,d) Fitted real permittivity of the BTO−Fe/BTO/mica and BTO−Fe/BTO−Au/mica films.

film reaches a maximum of $5 \times 10^{-10}$ A in the range of 0 to 15 V, suggesting a low leakage, especially under high voltage, which is desirable for ferroelectric applications. Additionally, the magnetoelectric coupling property was also measured for the BTO/BTO−Fe/BTO−Au/BTO/mica film, as plotted in Figure S8. As indicated by the slope of the linear fitted plot, the magnetoelectric coupling charge coefficient is found to be around $1.68 \times 10^{-7}$ $\mu$C/(cm$^2$ Oe). The magnetoelectric coupling from the strain-coupled nanocomposites paves new ways toward potential applications in flexible spintronics.

Considering the anisotropic structures of Fe pillars in the dielectric matrix, the optical properties of the films were characterized for the samples. Transmittance was first measured. In Figure 5a, the BTO−Fe/BTO−Au/mica film shows a plasmonic resonance peak around 512 nm, which is attributed to the existence of plasmonic Au nanostructures in the film. The plasmonic resonance peak position is also consistent with previous reports.[47,51,52] The transmittance measurement was also performed for the BTO−Fe/BTO−Au/mica film after the cyclic bending test and plotted in Figure 5b. The film shows a robust transmittance property at different bending conditions and post the cyclic bending test. The transmittance difference between different films is primarily due to their substrate thickness difference across different substrate pieces. Owing to the anisotropic nature of both films, the in-plane and out-of-plane permittivity was also measured by ellipsometry. The permittivity was attained by fitting the ellipsometric parameters Psi (Ψ) and Delta (Δ) using a uniaxial B-spline mode. The fitted real part permittivity of the films is summarized in Figure 5c,d. It can be seen that the out-of-plane permittivity is much lower than the in-plane permittivity for both films, which suggests the anisotropic dielectric properties of the VAN films, that is, more dielectric behavior in the in-plane direction. Interestingly, the BTO−Fe/BTO−Au/mica film shows a hyperbolic transition at around 700 nm, indicating a more metallic behavior in the out-of-plane direction for the BTO−Fe/BTO−Au/mica film, which also confirms that the BTO−Au-buffered film presents a better Fe pillar alignment and stronger out-of-plane structural anisotropy. The fitted imaginary permittivity of the films is summarized in Figure S9.

Overall, both films with different buffer layers promote successful growth of the BTO−Fe VAN, which also shows room-temperature multiferroic properties. Compared to previous single-phase oxides integration on mica, the BTO−Fe system exhibits a stronger magnetic anisotropy and better multifunctionality. The films on buffered mica substrates also show a comparable ferromagnetic property compared to those on rigid substrates, indicating a great potential for flexible device integration.[30,33] For future directions, other multiferroic nanocomposite systems could be considered to be integrated on mica substrates toward flexible electronics. For example, other metallic magnetic pillars (e.g., Co, Ni, etc.) and alloyed pillars (e.g., CoFe, $Au_xAg_{1-x}$, etc.) are ideal candidates to be


https://doi.org/10.1021/acsaelm.2c00712
ACS Appl. Electron. Mater. 2022, 4, 4077−4084

integrated on mica for multifunctional coupling. Moreover, further bending tests could be conducted to study how the bending radius would affect the microstructure and physical properties as well as the magnetoelectric coupling effect of the films. Furthermore, the mechanisms of buffer layers beneficial to thin-film integration on mica substrates need a further exploration, which can be extended to custom-designed and high-quality multifunctional oxide−metal VAN thin films.

## CONCLUSIONS

The BTO−Fe VAN system has been successfully integrated on flexible mica substrates. Different buffer layers (i.e., BTO and BTO−Au buffers) were introduced to facilitate the growth of the BTO−Fe VAN. In comparison, the BTO−Au interlayer promotes the growth quality of the Fe nanopillars better than the ones on the pure BTO buffer layer. The anisotropic ferromagnetic property and room-temperature ferroelectric property were observed for both films with either BTO or BTO−Au buffer layers. The BTO−Au-buffered film exhibits obvious plasmonic and hyperbolic properties. The physical properties of the films were stable even against the cyclic bending test. This work demonstrates the material feasibility for integrating multiferroic oxide−metal nanocomposite on mica toward multifunctionalities and flexible electronics.

## EXPERIMENTAL SECTION

**Thin Film Fabrication.** A BTO−Fe composite target with a molar ratio of 1:1 was used to deposit the thin film on the muscovite mica (001) substrate using pulsed laser deposition with a KrF laser (Lambda Physik Compex Pro 205, $\lambda$ = 248 nm). The chamber was pumped to the pressure of $2 \times 10^{-6}$ Torr before deposition. The temperature was maintained at 600 °C. After deposition, the chamber was cooled down to room temperature at a rate of 10 °C/min.

**Microstructure Characterization.** An FEI TALOS F200X microscope was used for TEM, STEM, and EDS characterization. X-ray diffraction was conducted using a Panalytical X'Pert X-ray diffractometer in the $\theta$−2$\theta$ scan mode.

**Magnetic Property Measurement.** The magnetic property measurement was conducted using a Quantum Design MPMS-3 SQUID magnetometer at room temperature.

**Ferroelectric Property Measurement.** The PFM measurement was carried out using atomic force microscopy (Bruker, Dimension Icon). The Radiant Technologies Precision LC II ferroelectric tester was used to perform the dielectric leakage tests. A $SrRuO_3$ layer was used as the bottom electrode, and Au contacts were used as the top electrodes for the ferroelectric test.

**Magnetoelectric Coupling Measurement.** The Radiant Technologies magnetoelectric bundle was employed to perform the magnetoelectric coupling measurement.

**Optical Property Measurement.** A UV−vis−NIR spectrophotometer (PerkinElmer Lambda 1050) was used for the transmittance property measurement in the wavelength range from 210 to 860 nm. The ellipsometry measurement was carried out using a J.A. Woollam RC2 ellipsometer.

## ASSOCIATED CONTENT

### Supporting Information

The Supporting Information is available free of charge at https://pubs.acs.org/doi/10.1021/acsaelm.2c00712.

HAADF STEM image for the nonbuffered film, EDS quantitative analysis, XRD $\theta$−2$\theta$ scan results, local regime of $M$−$H$ curves, polarization−voltage measurement result, PFM measurement results after cyclic bending, leakage current test result, magnetoelectric coupling property measurement result, and fitted imaginary permittivity of the two films (PDF)

## AUTHOR INFORMATION


### Corresponding Author

**Haiyan Wang** − *School of Materials Engineering and School of Electrical and Computer Engineering, Purdue University, West Lafayette, Indiana 47907, United States*; orcid.org/0000-0002-7397-1209; Email: hwang00@purdue.edu

### Authors

**Juncheng Liu** − *School of Materials Engineering, Purdue University, West Lafayette, Indiana 47907, United States*

**Xuejing Wang** − *School of Materials Engineering, Purdue University, West Lafayette, Indiana 47907, United States*

**Han Wang** − *School of Materials Engineering, Purdue University, West Lafayette, Indiana 47907, United States*; orcid.org/0000-0002-6137-4802

**Zhimin Qi** − *School of Materials Engineering, Purdue University, West Lafayette, Indiana 47907, United States*

**James P. Barnard** − *School of Materials Engineering, Purdue University, West Lafayette, Indiana 47907, United States*; orcid.org/0000-0002-7570-952X

**Bruce Zhang** − *School of Electrical and Computer Engineering, Purdue University, West Lafayette, Indiana 47907, United States*

Complete contact information is available at: https://pubs.acs.org/10.1021/acsaelm.2c00712


### Notes

The authors declare no competing financial interest.

## ACKNOWLEDGMENTS

This work was supported by the U.S. Department of Energy, Office of Science, Basic Energy Sciences (DE-SC0020077). This paper describes objective technical results and analysis. Any subjective views or opinions that might be expressed in the paper do not necessarily represent the views of the U.S. Department of Energy or the United States Government. X.W., Han Wang, and Haiyan Wang acknowledge the support from the U.S. National Science Foundation for the high-resolution microscopy effort (DMR-1565822 and DMR-2016453).

## REFERENCES

(1) Manipatruni, S.; Nikonov, D. E.; Lin, C. C.; Gosavi, T. A.; Liu, H.; Prasad, B.; Huang, Y. L.; Bonturim, E.; Ramesh, R.; Young, I. A. Scalable energy-efficient magnetoelectric spin-orbit logic. *Nature* **2019**, *565*, 35−42.

(2) Spaldin, N. A.; Ramesh, R. Advances in magnetoelectric multiferroics. *Nat. Mater.* **2019**, *18*, 203−212.

(3) Sun, N. X.; Srinivasan, G. Voltage Control of Magnetism in Multiferroic Heterostructures and Devices. *Spin*; World Scientific Publishing Company, September, 2012; Vol *02* (03), p 1240004.

(4) Lin, H.; Gao, Y.; Wang, X.; Nan, T.; Liu, M.; Lou, J.; Yang, G.; Zhou, Z.; Yang, X.; Wu, J.; Li, M.; Hu, Z.; Sun, N. X. Integrated magnetics and multiferroics for compact and power-efficient sensing, memory, power, RF, and microwave electronics. *IEEE Trans. Magn.* **2016**, *52*, 1−8.

(5) Ma, J.; Hu, J.; Li, Z.; Nan, C. W. Recent progress in multiferroic magnetoelectric composites: from bulk to thin films. *Adv. Mater.* **2011**, *23*, 1062−1087.

(6) Zhai, J.; Dong, S.; Xing, Z.; Li, J.; Viehland, D. Giant magnetoelectric effect in Metglas/polyvinylidene-fluoride laminates. *Appl. Phys. Lett.* **2006**, *89*, 083507.

(7) Gao, T.; Chen, Z.; Huang, Q.; Niu, F.; Huang, X.; Qin, L.; Huang, Y. A review: preparation of bismuth ferrite nanoparticles and its applications in visible-light induced photocatalyses. *Rev. Adv. Mater. Sci.* **2015**, *40*, 97−109.

(8) Catalan, G.; Scott, J. F. Physics and applications of bismuth ferrite. *Adv. Mater.* **2009**, *21*, 2463−2485.

(9) Hanamura, E.; Tanabe, Y. Phase transitions and second-harmonics of ferroelectric and antiferromagnetic $RMnO_3$. *Phase Transitions* **2006**, *79*, 957−971.

(10) Miyamoto, Y.; Ishiyama, K. Measurement of spontaneous electric polarization in magnetite ($Fe_3O_4$) at 4.2 K. *Solid State Commun.* **1993**, *87*, 581−583.

(11) Dutta, D. P.; Tyagi, A. K. Effect of $Sm^{3+}$ and $Zr^{4+}$ codoping on the magnetic, ferroelectric and magnetodielectric properties of sonochemically synthesized $BiFeO_3$ nanorods. *Appl. Surf. Sci.* **2018**, *450*, 429−440.

(12) Dutta, D. P.; Mandal, B. P.; Mukadam, M. D.; Yusuf, S. M.; Tyagi, A. K. Improved magnetic and ferroelectric properties of Sc and Ti codoped multiferroic nano $BiFeO_3$ prepared via sonochemical synthesis. *Dalton Trans.* **2014**, *43*, 7838−7846.

(13) Van Den Boomgaard, J.; Terrell, D. R.; Born, R. A. J.; Giller, H. F. J. I. An in situ grown eutectic magnetoelectric composite material. *J. Mater. Sci.* **1974**, *9*, 1705−1709.

(14) van den Boomgaard, J.; Born, R. A. J. A sintered magnetoelectric composite material $BaTiO_3$-Ni(Co, Mn)$Fe_2O_4$. *J. Mater. Sci.* **1978**, *13*, 1538−1548.

(15) Vaz, C. A.; Hoffman, J.; Ahn, C. H.; Ramesh, R. Magnetoelectric coupling effects in multiferroic complex oxide composite structures. *Adv. Mater.* **2010**, *22*, 2900−2918.

(16) Nan, C. W.; Bichurin, M. I.; Dong, S.; Viehland, D.; Srinivasan, G. Multiferroic magnetoelectric composites: Historical perspective, status, and future directions. *J. Appl. Phys.* **2008**, *103*, 1.

(17) Zheng, H.; Wang, J.; Lofland, S. E.; Ma, Z.; Mohaddes-Ardabili, L.; Zhao, T.; Salamanca-Riba, L.; Shinde, S. R.; Ogale, S. B.; Bai, F.; Viehland, D.; Jia, Y.; Schlom, D. G.; Wuttig, M.; Roytburd, A.; Ramesh, R. Multiferroic batio3-cofe2o4 nanostructures. *Science* **2004**, *303*, 661−663.

(18) Wang, J. B. N. J.; Neaton, J. B.; Zheng, H.; Nagarajan, V.; Ogale, S. B.; Liu, B.; Viehland, D.; Vaithyanathan, V.; Schlom, D. G.; Waghmare, U. V.; Spaldin, N. A.; Rabe, K. M.; Wuttig, M.; Ramesh, R. Epitaxial BiFeO3 multiferroic thin film heterostructures. *science* **2003**, *299*, 1719−1722.

(19) Rutherford, B. X.; Zhang, B.; Kalaswad, M.; He, Z.; Zhang, D.; Wang, X.; Liu, J.; Wang, H. Tunable Three-Phase Co−CeO2−BaTiO3 Hybrid Metamaterials with Nano-Mushroom-Like Structure for Tailorable Multifunctionalities. *ACS Appl. Nano Mater.* **2022**, *5*, 6297−6304.

(20) Lebedev, O. I.; Verbeeck, J.; Van Tendeloo, G.; Shapoval, O.; Belenchuk, A.; Moshnyaga, V.; Damashcke, B.; Samwer, K. Structural phase transitions and stress accommodation in $(La_{0.67}Ca_{0.33}MnO_3)_{1-x}:(MgO)_x$ composite films. *Phys. Rev. B* **2002**, *66*, 104421.

(21) MacManus-Driscoll, J. L.; Zerrer, P.; Wang, H.; Yang, H.; Yoon, J.; Fouchet, A.; Yu, R.; Blamire, M. G.; Jia, Q. Strain control and spontaneous phase ordering in vertical nanocomposite heteroepitaxial thin films. *Nat. Mater.* **2008**, *7*, 314−320.

(22) Chen, A.; Bi, Z.; Hazariwala, H.; Zhang, X.; Su, Q.; Chen, L.; Jia, Q.; MacManus-Driscoll, J. L.; Wang, H. Microstructure, magnetic, and low-field magnetotransport properties of self-assembled $(La_{0.7}Sr_{0.3}MnO_3)_{0.5}:(CeO_2)_{0.5}$ vertically aligned nanocomposite thin films. *Nanotechnology* **2011**, *22*, 315712.

(23) Li, L.; Misra, S.; Gao, X.; Liu, J.; Wang, H.; Huang, J.; Zhang, B.; Lu, P.; Wang, H. Novel vertically aligned nanocomposite of Bi2WO6-Co3O4 with room-temperature multiferroic and anisotropic optical response. *Nano Res.* **2021**, *14*, 4789−4794.

(24) Li, L.; Sun, L.; Gomez-Diaz, J. S.; Hogan, N. L.; Lu, P.; Khatkhatay, F.; Zhang, W.; Jian, J.; Huang, J.; Su, Q.; Fan, M.; Jacob, C.; Li, J.; Zhang, X.; Jia, Q.; Sheldon, M.; Alù, A.; Li, X.; Wang, H. Self-Assembled Epitaxial Au-Oxide Vertically Aligned Nanocomposites for Nanoscale Metamaterials. *Nano Lett.* **2016**, *16*, 3936−3943.

(25) Wang, X.; Choi, J.; Liu, J.; Malis, O.; Li, X.; Bermel, P.; Zhang, X.; Wang, H. 3D Hybrid Trilayer Heterostructure: Tunable Au Nanorods and Optical Properties. *ACS Appl. Mater. Interfaces* **2020**, *12*, 45015−45022.

(26) Wang, X.; Qi, Z.; Liu, J.; Wang, H.; Xu, X.; Zhang, X.; Wang, H. Strong Interfacial Coupling of Tunable Ni−NiO Nanocomposite Thin Films Formed by Self-Decomposition. *ACS Appl. Mater. Interfaces* **2021**, *13*, 39730.

(27) Lu, J.; Paldi, R. L.; Pachaury, Y.; Zhang, D.; Wang, H.; Kalaswad, M.; Sun, X.; Liu, J.; Phuah, X. L.; Zhang, X.; El-Azab, A. A.; Wang, H. Ordered hybrid metamaterial of $La_{0.7}Sr_{0.3}MnO_3$−Au vertically aligned nanocomposites achieved on templated $SrTiO_3$ substrate. *Mater. Today Nano* **2021**, *15*, 100121.

(28) Huang, J.; Zhang, D.; Liu, J.; Dou, H.; Wang, H. Double-Exchange Bias Modulation under Horizontal and Perpendicular Field Directions by 3D Nanocomposite Design. *ACS Appl. Mater. Interfaces* **2021**, *13*, 50141−50148.

(29) Wang, X.; Jian, J.; Wang, H.; Liu, J.; Pachaury, Y.; Lu, P.; Rutherford, B. X.; Gao, X.; Xu, X.; El-Azab, A.; Zhang, X.; Wang, H. Nitride-Oxide-Metal Heterostructure with Self-Assembled Core−Shell Nanopillar Arrays: Effect of Ordering on Magneto-Optical Properties. *Small* **2021**, *17*, 2007222.

(30) Zhang, B.; Huang, J.; Rutherford, B. X.; Lu, P.; Misra, S.; Kalaswad, M.; He, Z.; Gao, X.; Sun, X.; Li, L.; Wang, H. Tunable, room-temperature multiferroic Fe-$BaTiO_3$ vertically aligned nanocomposites with perpendicular magnetic anisotropy. *Mater. Today Nano* **2020**, *11*, 100083.

(31) Zhang, W.; Chen, A.; Jian, J.; Zhu, Y.; Chen, L.; Lu, P.; Jia, Q.; MacManus-Driscoll, J. L.; Zhang, X.; Wang, H. Strong perpendicular exchange bias in epitaxial $La_{0.7}Sr_{0.3}MnO_3$:$BiFeO_3$ nanocomposite films through vertical interfacial coupling. *Nanoscale* **2015**, *7*, 13808−13815.

(32) Kalaswad, M.; Zhang, B.; Wang, H.; Wang, X.; Huang, J.; Wang, H. Tailorable Fe nanostructures and magnetic anisotropy in $(La_{0.5}Sr_{0.5}FeO_3)_{1-x}:Fe_x$ thin films integrated on $SrTiO_3$ and silicon substrates. *Mater. Today Adv.* **2020**, *8*, 100112.

(33) Kalaswad, M.; Zhang, B.; Wang, X.; Wang, H.; Gao, X.; Wang, H. Integration of highly anisotropic multiferroic $BaTiO_3$−Fe nanocomposite thin films on Si towards device applications. *Nanoscale Adv.* **2020**, *2*, 4172−4178.

(34) Yamamoto, Y.; Harada, S.; Yamamoto, D.; Honda, W.; Arie, T.; Akita, S.; Takei, K. Printed multifunctional flexible device with an integrated motion sensor for health care monitoring. *Sci. Adv.* **2016**, *2*, No. e1601473.

(35) Rogers, J. A.; Someya, T.; Huang, Y. Materials and mechanics for stretchable electronics. *Science* **2010**, *327*, 1603−1607.

(36) Bao, Z.; Chen, X. Flexible and Stretchable Devices. *Adv. Mater.* **2016**, *28*, 4177−4179.

(37) Gao, W.; Emaminejad, S.; Nyein, H. Y. Y.; Challa, S.; Chen, K.; Peck, A.; Fahad, H. M.; Ota, H.; Shiraki, H.; Kiriya, D.; Lien, D. H.; Brooks, G. A.; Davis, R. W.; Javey, A. Fully integrated wearable sensor arrays for multiplexed in situ perspiration analysis. *Nature* **2016**, *529*, 509−514.

(38) Son, D.; Lee, J.; Qiao, S.; Ghaffari, R.; Kim, J.; Lee, J. E.; Song, C.; Kim, S. J.; Lee, D. J.; Jun, S. W.; Yang, S.; Park, M.; Shin, J.; Do, K.; Lee, M.; Kang, K.; Hwang, C. S.; Lu, N.; Hyeon, T.; Kim, D.-H. Multifunctional wearable devices for diagnosis and therapy of movement disorders. *Nat. Nanotechnol.* **2014**, *9*, 397−404.

(39) Gustafsson, G.; Cao, Y.; Treacy, G. M.; Klavetter, F.; Colaneri, N.; Heeger, A. J. Flexible light-emitting diodes made from soluble conducting polymers. *Nature* **1992**, *357*, 477−479.

(40) Kim, H.; Kim, Y.; Kim, K. S.; Jeong, H. Y.; Jang, A. R.; Han, S. H.; Yoon, D. H.; Suh, K. S.; Shin, H. S.; Kim, T.; Yang, W. S. Flexible thermochromic window based on hybridized VO2/graphene. *ACS Nano* **2013**, *7*, 5769−5776.

(41) Huang, J.; Zhang, D.; Liu, J.; Wang, H. Freestanding $La_{0.7}Sr_{0.3}MnO_3$:NiO vertically aligned nanocomposite thin films for

flexible perpendicular interfacial exchange coupling. *Mater. Res. Lett.* **2022**, *10*, 287–294.
(42) Xu, R.; Zhang, X.; Zhang, D.; Liu, J.; Lu, J.; Zhao, R.; Ji, Y.; Qian, F.; Wang, H.; Fan, J.; Li, W.; Yang, H. High stability of flexible perovskite transparent conductive oxide film via van der Waals heteroepitaxy. *J. Alloys Compd.* **2022**, *890*, 161897.
(43) Jiang, J.; Bitla, Y.; Huang, C. W.; Do, T. H.; Liu, H. J.; Hsieh, Y. H.; Ma, C. H.; Jang, C. Y.; Lai, Y. H.; Chiu, P. W.; Wu, W. W.; Chen, Y. C.; Zhou, Y. C.; Chu, Y. H. Flexible ferroelectric element based on van der Waals heteroepitaxy. *Sci. Adv.* **2017**, *3*, No. e1700121.
(44) Chu, Y. H. Van der Waals oxide heteroepitaxy. *npj Quantum Mater.* **2017**, *2*, 1–5.
(45) Amrillah, T.; Bitla, Y.; Shin, K.; Yang, T.; Hsieh, Y. H.; Chiou, Y. Y.; Liu, H. J.; Do, T. H.; Su, D.; Chen, Y. C.; Jen, S. U.; Chen, L.-Q.; Kim, K. H.; Juang, J.-Y.; Chu, Y.-H. Flexible multiferroic bulk heterojunction with giant magnetoelectric coupling via van der Waals epitaxy. *ACS Nano* **2017**, *11*, 6122–6130.
(46) Huang, J.; Wang, H.; Wang, X.; Gao, X.; Liu, J.; Wang, H. Exchange Bias in a $La_{0.67}Sr_{0.33}MnO_3$/NiO Heterointerface Integrated on a Flexible Mica Substrate. *ACS Appl. Mater. Interfaces* **2020**, *12*, 39920–39925.
(47) Liu, J.; Wang, X.; Gao, X.; Wang, H.; Jian, J.; Huang, J.; Sun, X.; Qi, Z.; Misra, S.; He, Z.; Wang, H. Multifunctional self-assembled $BaTiO_3$-Au nanocomposite thin films on flexible mica substrates with tunable optical properties. *Appl. Mater. Today* **2020**, *21*, 100856.
(48) Liu, J.; Wang, X.; Gao, X.; Wang, H.; Zhang, B.; Zhang, D.; Kalaswad, M.; Huang, J.; Wang, H. Integration of Self-Assembled $BaZrO_3$-Co Vertically Aligned Nanocomposites on Mica Substrates toward Flexible Spintronics. *Cryst. Growth Des.* **2021**, *22*, 718–725.
(49) Dutta, D. P.; Roy, M.; Maiti, N.; Tyagi, A. K. Phase evolution in sonochemically synthesized $Fe^{3+}$ doped $BaTiO_3$ nanocrystallites: structural, magnetic and ferroelectric characterisation. *Phys. Chem. Chem. Phys.* **2016**, *18*, 9758–9769.
(50) Wu, J.; Liang, Z.; Ma, C.; Hu, G.; Shen, L.; Sun, Z.; Zhang, Y.; Lu, L.; Liu, M.; Jia, C. L. Flexible lead-free $BaTiO_3$ ferroelectric elements with high performance. *IEEE Electron Device Lett.* **2019**, *40*, 889–892.
(51) Zhang, D.; Misra, S.; Li, L.; Wang, X.; Jian, J.; Lu, P.; Gao, X.; Sun, X.; Qi, Z.; Kalaswad, M.; Zhang, X.; Wang, H. Tunable Optical Properties in Self-Assembled Oxide-Metal Hybrid Thin Films via Au-Phase Geometry Control: From Nanopillars to Nanodisks. *Adv. Opt. Mater.* **2020**, *8*, 1901359.
(52) Zhang, D.; Lu, P.; Misra, S.; Wissel, A.; He, Z.; Qi, Z.; Gao, X.; Sun, X.; Liu, J.; Lu, J.; Zhang, X.; Wang, H. Design of 3D Oxide–Metal Hybrid Metamaterial for Tailorable Light–Matter Interactions in Visible and Near-Infrared Region. *Adv. Opt. Mater.* **2021**, *9*, 2001154.

## Recommended by ACS

**Ultrahigh Ferroelectric and Piezoelectric Properties in $BiFeO_3$–$BaTiO_3$ Epitaxial Films Near Morphotropic Phase Boundary**

Yu-Qing Hu, Chun-Gang Duan, *et al.*
AUGUST 05, 2022
ACS APPLIED MATERIALS & INTERFACES
READ

**Control of Layering in Aurivillius Phase Nanocomposite Thin Films and Influence on Ferromagnetism and Optical Absorption**

Lutz Mühlenbein, Akash Bhatnagar, *et al.*
APRIL 12, 2022
ACS APPLIED ELECTRONIC MATERIALS
READ

**Paraelectric Matrix-Tuned Energy Storage in $BiFeO_3$–$BaTiO_3$–$SrTiO_3$ Relaxor Ferroelectrics**

Wei Wang, Yan-Ping Jiang, *et al.*
AUGUST 18, 2021
ACS APPLIED ENERGY MATERIALS
READ

**Ferroelectric Multilayer Nanocomposites with Polarization and Stress Concentration Structures for Enhanced Triboelectric Performances**

Yoojeong Park, Hyunhyub Ko, *et al.*
JUNE 05, 2020
ACS NANO
READ

**Get More Suggestions >**


https://doi.org/10.1021/acsaelm.2c00712
*ACS Appl. Electron. Mater.* 2022, 4, 4077–4084